Bias Tunable Spectral Response of Nanocrystal Array in a Plasmonic Cavity

Tung Huu Dang, Angela Vasanelli, Yanko Todorov, Carlo Sirtori, Yoann Prado, Audrey Chu, Charlie Gréboval, Adrien Khalili, Herve Cruguel, Christophe Delerue, et al.

Bias Tunable Spectral Response of Nanocrystal Array in a Plasmonic Cavity

Tung Huu Dang[1,2], Angela Vasanelli[1*], Yanko Todorov[1], Carlo Sirtori[1], Yoann Prado[2], Audrey Chu[2,3], Charlie Gréboval[2], Adrien Khalili[2], Herve Cruguel[2], Christophe Delerue[4], Gregory Vincent[3], Emmanuel Lhuillier[2*]

[1] Laboratoire de physique de l'Ecole Normale Supérieure, ENS, Université PSL, CNRS, Sorbonne Université, Université de Paris, 75005 Paris, France
[2] Sorbonne Université, CNRS, Institut des NanoSciences de Paris, INSP, 75005 Paris, France.
[3] ONERA - The French Aerospace Lab, 6, chemin de la Vauve aux Granges, BP 80100, 91123 Palaiseau, France.
[4]Univ. Lille, CNRS, Centrale Lille, Univ. Polytechnique Hauts-de-France, Junia, UMR 8520 - IEMN, F-59000 Lille, France

Abstract: Nanocrystals (NCs) have gained considerable attention for their broadly tunable absorption from the UV to the THz range. Nevertheless, their optical features suffer from a lack of tunability once integrated into optoelectronic devices. Here, we show that tunable absorption with bias can be obtained by coupling a HgTe NC array with a plasmonic resonator. Up to 15 meV blueshift can be achieved from a 3-µm absorbing wavelength structure under a 3 V bias voltage when the NC exciton is coupled with a mode of the resonator. We demonstrate that the blueshift arises from the interplay between hopping transport and inhomogeneous absorption due to the presence of the photonic structure. The observed tunable spectral response is qualitatively reproduced in simulation by introducing a bias-dependent diffusion length in the charge transport. This work expands the realm of existing NC-based devices and paves the way towards light modulators.

Keywords: *plasmon, hopping transport, nanocrystal, bias-induced spectral shift, infrared.*

*To whom correspondence should be sent: angela.vasanelli@ens.fr and el@insp.upmc.fr

Introduction

While nanocrystals (NCs) are claimed for being essential building blocks for optoelectronic devices, the actual number of devices based on these colloidal nanoparticles remains mostly limited to solar cells,[1–3] light-emitting diodes,[4,5] and, more recently, infrared focal plane arrays.[6–8] Thus, many concepts of devices remain unexplored in the case of colloidal NCs.

One of the most striking successes of NCs comes from their broad spectral tunability. By combining quantum confinement to the extensive library of materials that can be grown under the colloidal form, a significant part of the electromagnetic spectrum - from UV to THz[9] - can be addressed. However, once integrated into a device, their spectral response is set by the choice of the synthesis parameters. This limitation can be overcome by engineering the light-matter coupling with light resonators and cavities.[10,11] This approach has been used to design spectral filters,[12] as well as to broaden the absorption[13] of NC thin films.[14,15] While this strategy offers post-synthesis tunability, this remains a non-agile method, where device geometrical factors now determine the spectral response.

Nevertheless, reconfigurable responses are still of utmost interest not only for light sensing and emission[16] but also for devices such as light modulators. Several strategies to achieve a reconfigurable spectral response have been explored: exploiting the Stark effect,[17] with a redshift of the band edge under an electric field application,[18–21] or electrochromism, by charging the NC film.[22] The field required to induce a tunable response is extremely large, typically above 100 $kV.cm^{-1}$. This strong electric field is generally not compatible with electrical transport due to electrical breakdowns. As a result, only the optical features can be tuned by these approaches. More recently, reconfigurable spectral responses have been obtained from phase change materials[23,24] and MEMS actuators,[25] but these strategies are not straightforward to be applied to NC-based films.

Here, we design a spectrally tunable NC-based device by carefully coupling the electromagnetic field and the charge collection resulting from hopping within a NC assembly. To build such a device, we combine a HgTe NC[26] thin-film absorbing in the extended short-wave infrared (e-SWIR) with a plasmonic resonator. The latter induces a spatially inhomogeneous spectral response within the device. We show that, by applying a small electric field (<40 $kV.cm^{-1}$), the spectral response of the photodetector is shifted up to 15 meV.

Results and discussion

We design a device based on HgTe NCs. The latter are grown using the Prado *et al.* procedure.[27] Briefly, $HgBr_2$ and TOP:Te are mixed at room temperature and react to form seeds that later grow when heated in a hot oleylamine solution. TEM observations (**Figure 1**b and S1) show that the obtained particles have a slightly faceted spherical shape, with a typical diameter close to 10 nm. The resulting absorption spectrum (**Figure 1**b) shows an exciton resonance at 4200 cm^{-1} (≈2.4 µm) and a narrow doublet at 2900 cm^{-1} resulting from the C-H bond resonance of the capping ligands. The plasmonic cavity is fabricated on a sapphire substrate to ensure good transparency in the 1-3 µm range, see figure S2-5 for design and S7-9 for fabrication. On top of the substrate, a gold grating is fabricated by e-beam lithography, as sketched in **Figure 1**a. The period *p* of the grating is chosen so that a surface plasmon polariton resonance overlaps with the HgTe NC exciton one when it is excited in the vicinity of the first diffraction order of the grating[28]. The refractive index of HgTe NCs film being 2.35,[29] *p* is estimated to be around 1350 nm.[28] This grating is also used as interdigitated electrodes: bias is applied between two adjacent electrodes to generate photocurrent. The NC film is deposited on the top of the grating by spin-coating an ink containing HgTe particles capped with $HgCl_2$ and short thiols. Atomic force microscopy (Figure S9) reveals that NC deposition on the grating is quasi-conformal. Finally, a top gold layer is added to generate the spoof surface plasmon whose wavelength is selected by the bottom grating period. A thin PMMA (20 nm) layer is added between the NC film and the top electrode to be used as a gate and controls the NC film carrier density.

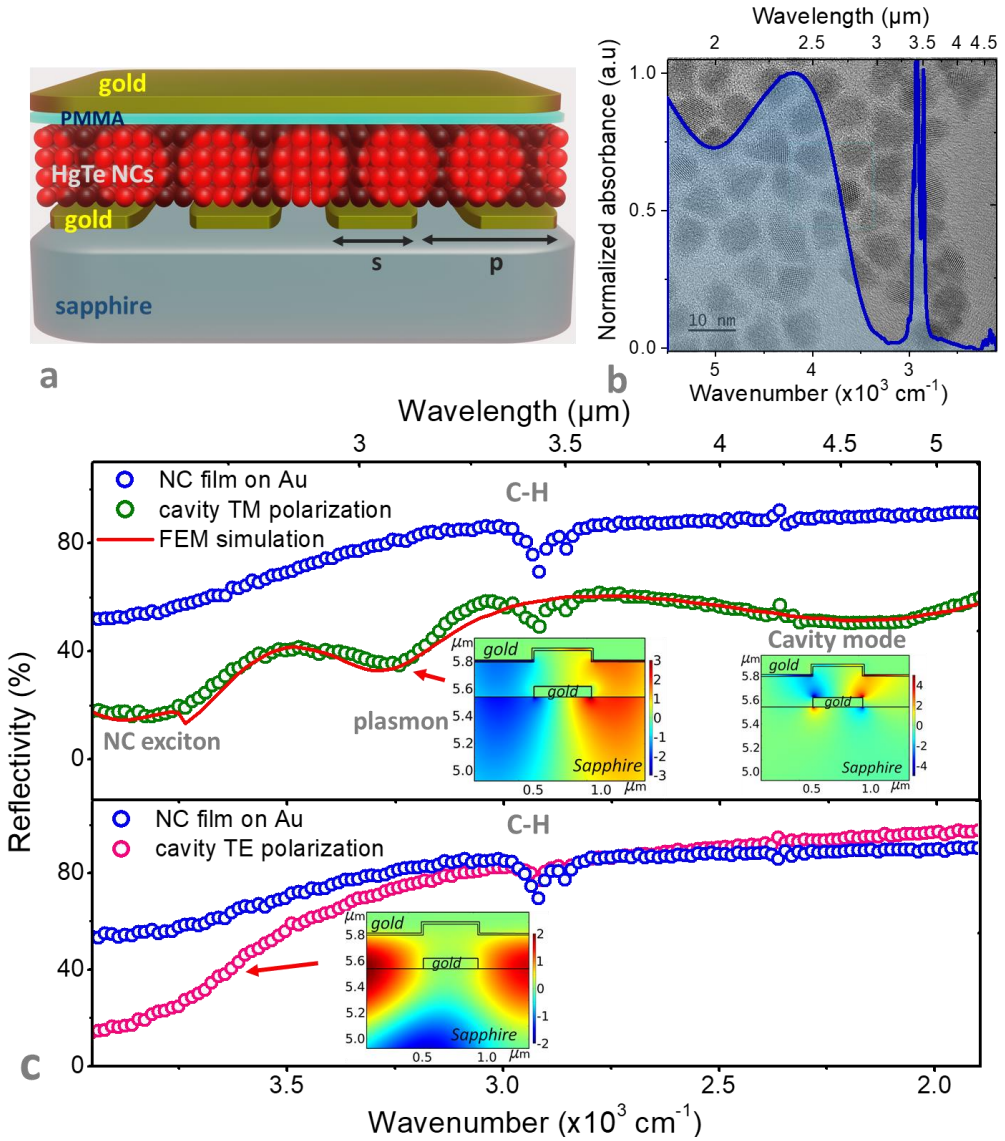

Figure 1: HgTe NCs coupled to plasmonic resonator*. a. Schematic of the plasmonic resonator coupled to a HgTe NC film. b. Room temperature absorption spectrum of the HgTe NCs. The background is a transmission electron microscopy image of those HgTe NCs. c. Experimental reflectivity spectra measured at room temperature and at 15° incidence angle for a NC film deposited on a gold layer (blue circles), and for the device depicted in part a with s = 500 nm and p = 1350 nm. The top panel presents the experimental (green circles) and simulated (red line) reflectivity spectrum with TM polarized radiation, the bottom one presents the experimental spectrum in TE polarization. The inset also shows the electric field map associated with the resonance at 3200 cm^{-1} (spoof surface plasmon resonance) and 2160 cm^{-1} (patch cavity mode) in TM polarization, and in correspondence to the broad feature observed in TE.*

Figure 1c presents the optical properties of our device by comparing the reflectivity of a nanocrystal film deposited on a gold layer (blue symbols) to the reflectivity of the device in TM (top panel) and TE (bottom panel) polarizations, measured at the incident angle of 15°. At 3800 cm^{-1}, we observe the HgTe exciton. The peak is shifted compared to the value measured in solution due to interparticle coupling generated by the ligand exchange and change of dielectric environment. The coupling with the first diffraction order of the grating enhances the contrast of the exciton resonance in both polarizations. We have verified that this enhancement corresponds to an increased absorptivity induced by the cavity (see Figure S3a). The optical properties of the device are dependent on the light polarization. In the case of the TM polarization, a second feature appears at 3300 cm^{-1} in the tail of the absorption of the NCs. This resonance is associated with a surface plasmon polariton mode supported by the gold, nanocrystal, sapphire multilayer, excited in the vicinity of the first diffraction order of the grating. As discussed later, the inhomogeneous spatial distribution of the

modes will play a central role in achieving bias tunability of the photoresponse. Note that the plasmon mode has a strong dispersion (see Figure S2c), and at normal incidence, it is shifted towards the excitonic peak. At 2200 cm^{-1}, corresponding to $\lambda=2.n_{effective}.s$ with $n_{effective}$ the cavity effective index and s the patch size, a weak and broad dip appears. This feature is associated with a resonance of the patch cavity formed between the top and bottom gold electrodes[30] (right inset of **Figure 1**c, top panel, and Figure S5).

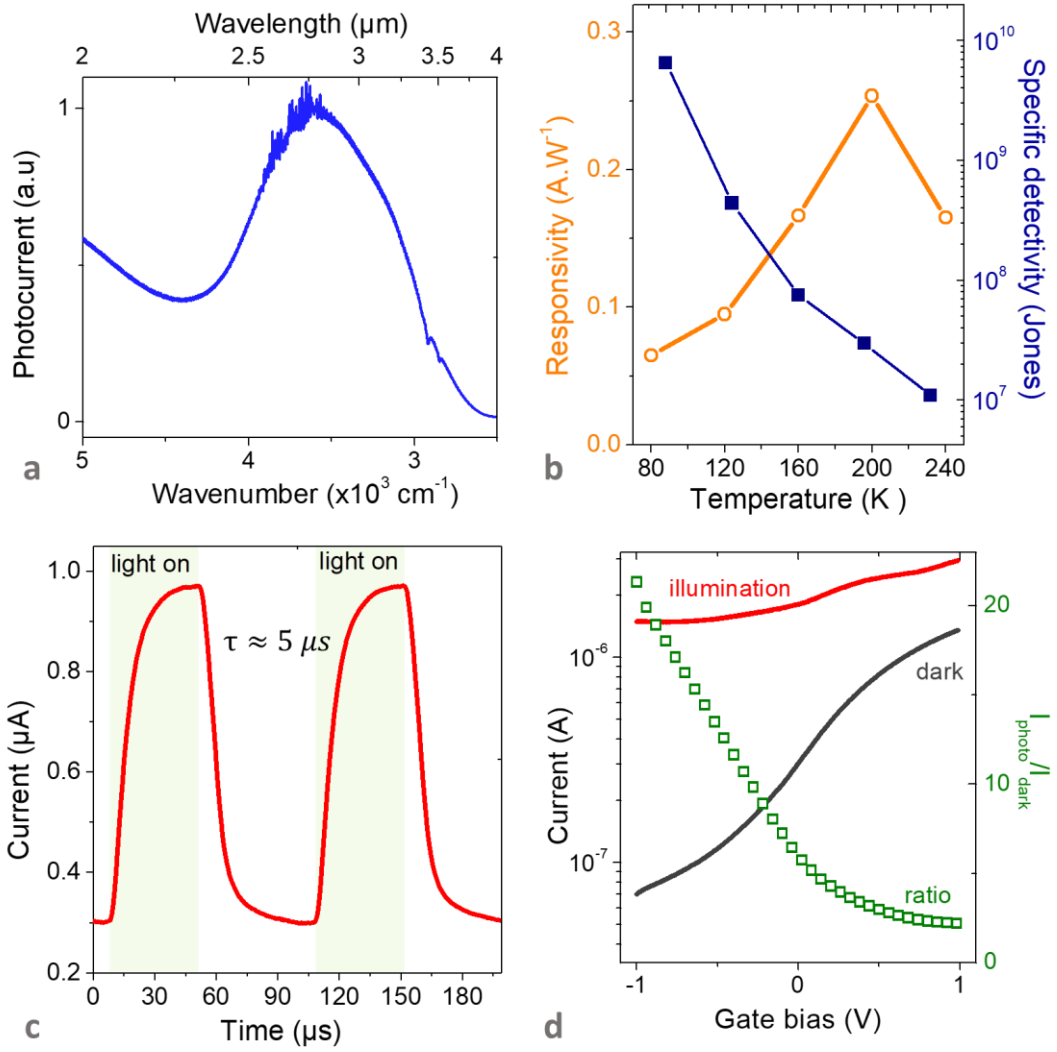

***Figure 2: Detection performance**. a. Photocurrent spectra under unpolarized illumination at 80 K for the film in the plasmonic cavity. b. Responsivity (under blackbody illumination at 980 °C) and detectivity (at 1 kHz) as a function of operating temperature for V_{DS}=0.5 V. c. Current as a function of time while the light (λ=1.55 µm) is turned on and off. d. Currents (dark and under illumination) as a function of gate bias, for V_{DS}=0.2 V, at 150 K. The ratio of those two currents is plotted on the right axis as a function of the gate bias.*

The designed device presents photoconductive properties, see ***Figure 2***a and S10-15 for characterization. The introduction of the resonator clearly affects the spectral response of the device. A more pronounced photocurrent peak is observed in the plasmonic resonator device (with p=1.5 µm) with respect to a reference device in which the NC film is connected to conventional interdigitated electrodes (*i.e.,* no top gold layer), separated by a period of 20 µm, see figure S3b. In terms of detection performance, the device responsivity under broadband illumination (blackbody at 980 °C) reaches 0.25 $A.W^{-1}$ at 200 K (***Figure 2***b), corresponding to an external quantum efficiency EQE≈20%. Below this temperature, the responsivity drops due to the thermal activation of the mobility.[15] Simultaneously the carrier density is also thermally activated, thus the dark current can be drastically reduced thanks to cooling (see figure S15). Consequently, the prevailing *1/f* noise

current spectral density drops with temperature (Figure S13), and the specific detectivity increases from 10^7 Jones at 240 K to $8x10^9$ Jones at 80 K, see ***Figure 2***b. The time response of the device, as presented in ***Figure 2***c, is around 5 µs, which is quite typical for devices based on HgTe NCs.[26]
The top gate (PMMA) can be used to control the device carrier density. ***Figure 2***d reports the dark current (black line) and the current under illumination (red line) as a function of the gate bias. The dark conduction increases as a larger positive gate bias voltage is applied, indicating the n-type nature of the HgTe NC channel. This result is consistent with the measurement conducted with an electrolyte gated field-effect transistor configuration, see Figure S16. By applying a negative gate bias, the majority carriers are removed from the channel, and the film becomes more intrinsic, leading to an increase of the photocurrent to dark current ratio up to a factor of 20 (green symbols).
The most striking feature of this device is its bias tunable photoresponse, see **Figure 3**a. As a bias is applied between the two channel electrodes, a blueshift of the photoresponse is observed. This blue shift is present in both TM and TE polarizations (see Figure S17 and S18) and is fully reversible when bias is suppressed. Note that the blue shift is observed for both bias polarities (see Figure S19). This blue shift is somehow counterintuitive: usually, applying an electric field on quantum-confined semiconductors leads to a redshift as the wavefunction starts to leak in the barriers. Using tight-binding simulations, we have checked that a redshift should indeed be observed in HgTe NCs under electric field, see Figure S6. However, the calculated magnitude of this redshift is very weak. Tight-binding simulations predict a 6 cm^{-1} (<1 meV) shift under 100 $kV.cm^{-1}$ applied electric field, while we observe an inverted shift reaching more than 15 meV under 40 $kV.cm^{-1}$ (3 V over 0.85 µm electrode spacing) at 50 K, see **Figure 3**b. We can conclude that the observed shift is not induced by an effect of the electric field on the electronic states of the NCs.
HgTe NCs present an inverted temperature dependence of the bandgap, leading to a blueshift of the bandgap upon heating. To quantify this effect, we performed a series of photocurrent spectra at various temperatures and found a 120 $\mu eV.K^{-1}$ value for dEg/dT, see Figure S21. As a bias is applied, the current flowing within the device may generate heat due to Joule effect. However, the 15 meV observed shift would correspond to an increase of 120 K in temperature, which is improbable to be induced by the small Joule dissipated power ($RI^2 \approx$ a few nW under 1 V bias << several mW cooling power of the cryocooler at 80 K) in our device at low temperatures. Moreover, this heating should be more critical when the device resistance is reduced (*i.e.,* at higher temperatures), while in our device, the opposite trend is observed (*i.e.,* more noticeable shift as temperature decreases), see **Figure 3**b.
We then use the gate to see its impact on the spectrum, see **Figure 3**c. In this case, no shift is observed while the magnitude of the gate-induced electric field (1 V over 20 nm of PMMA) corresponds to 500 $kV.cm^{-1}$, which is one order of magnitude larger than the drain-source electric field applied to generate the shift. As a consequence, the observed shift cannot be induced by a variation of the carrier density.

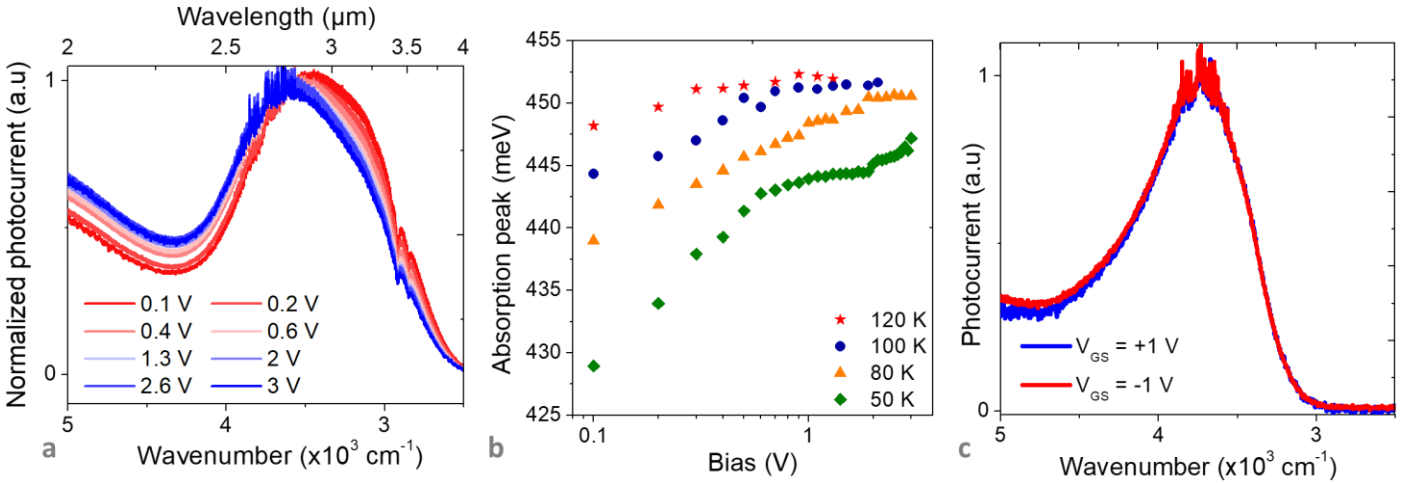

Figure 3: Bias-induced spectral shift*. a. Photocurrent spectra for non-polarized light under various applied bias voltages. b. Energy of the first photocurrent peak as a function of the applied bias for various operating temperatures. c. Photocurrent spectra for non-polarized light for two different gate bias voltages.*

In order to understand the origin of the blueshift of the photocurrent spectrum, it should be pointed out that no shift is observed for a HgTe film on conventional interdigitated (no cavity, no plasmon) electrodes under bias voltage application, see Figure S14. Furthermore, even devices with smaller electrode spacing, with ≈50 nm separation between the electrodes, and consequently with even larger applied electric fields, do not present such a bias dependence of the photocurrent spectrum[31]. Therefore, it is suggested that the special device architecture, generating a specific light-matter coupling, is at the origin of this spectral response tunability. The simulated absorption maps, obtained as described in section S3 of the SI, reveal this coupling for TM (**Figure 4**a) and TE polarizations (Figure S4a). In both cases, the absorption maps appear to be strongly inhomogeneous. In particular, the NC absorption is concentrated between, rather than above, the electrodes of the grating. The areas between the electrodes (region 1 of **Figure 4**a) present a maximum of the NC absorption strongly blue-shifted compared to those above the electrodes (region 2 of **Figure 4**a). Away from the cavity, when field enhancement is weak, the spectrum is driven by the NC film only. In the cavity, the field magnitude is enhanced and the plasmon resonance is spectrally overlapping with the exciton. As seen from **Figure 1**c and Figure S3 b, the plasmon has been chosen to be slightly detuned compared to the exciton, thus enhancing the red part of the NC spectrum. As a result, we have coupled the field enhancement with the redshifted spectrum, see **Figure 4**b.

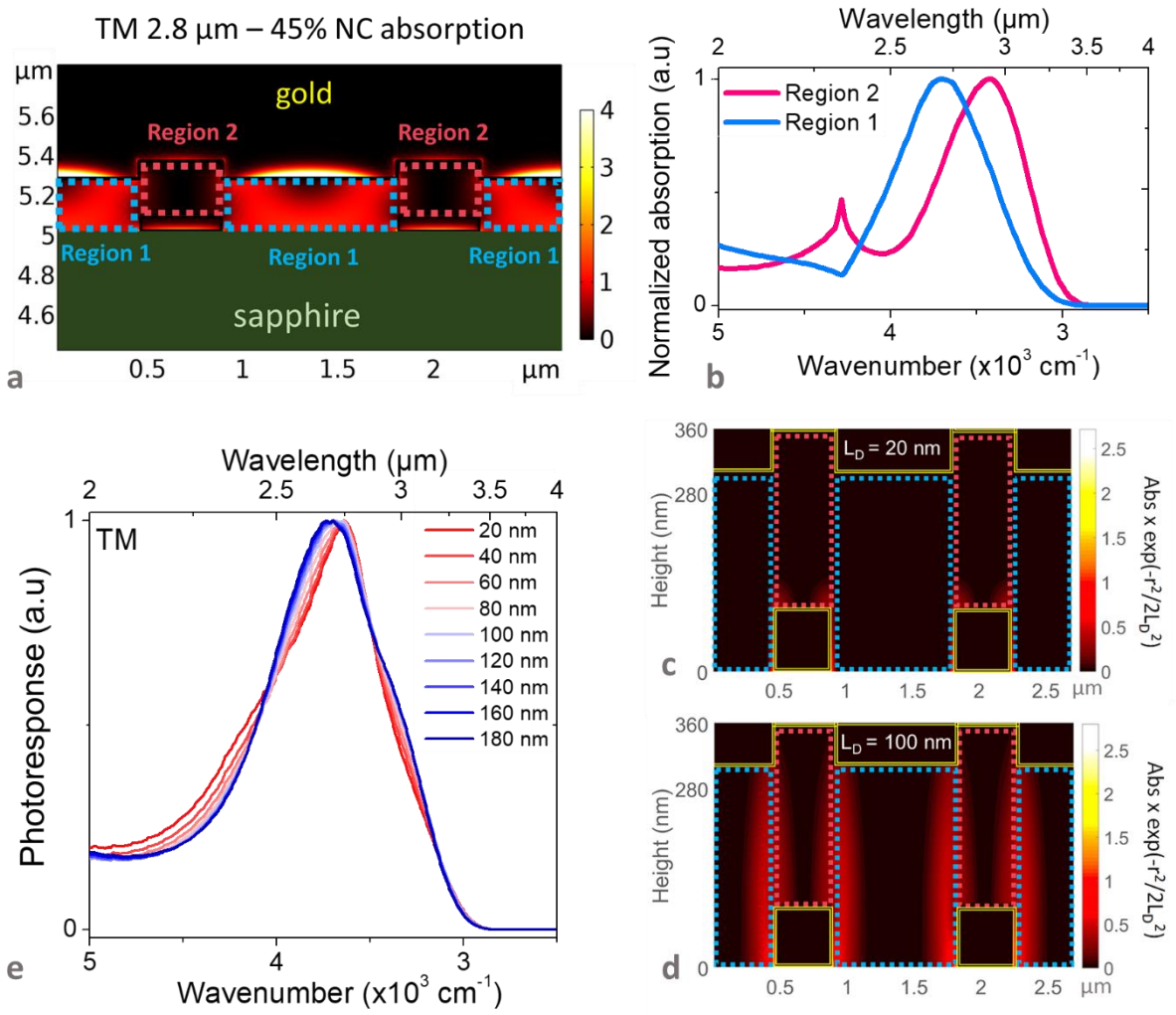

Figure 4: Origin of the bias-induced shift for TM polarization*. a. Simulated absorption map for the TM polarization. For the device depicted in* ***Figure 1****a, we define two zones: region 1 is between electrodes, while region 2 is above electrodes. b. Simulated absorption spectra in region 1 and 2 defined on part a. c. (resp. d.) Product of the absorbance by exp(-r²/2L_D²), with r the distance to the electrode while L_D is set equal to 20 nm (resp. 100 nm). e. Normalized photoresponse (calculated by* $\iint_{NC\ film} Abs(r,\lambda).exp\left(-\frac{r^2}{2L_D^2}\right) dS$*, with dS is surface element) for various L_D values. Data for TE mode are given in figure S4.*

Due to the polycrystalline nature of the film, the transport occurs through a hopping process, leading to short diffusion lengths of the order of a few tens of nm.[31] In a field-assisted hopping model,[32–35] the diffusion coefficient can be written $D(F,T)= D_0(T)+A(F,T).F^2$ (1), where $D_0(T)$ is the diffusion coefficient in the zero-field limit, *F is* the magnitude of the electric field, and $A(F,T)$ is a coupling factor. This diffusion coefficient directly relates the diffusion length with the carrier lifetime τ through $L_D(F,T) = \sqrt{D(F,T)\cdot\tau}$. We see from equation (1) that the application of a bias tends to increase the diffusion length. Thus, carriers that are photogenerated further away from the electrodes can be collected. As a result, the weight from the absorption occurring in region 1 becomes more important, leading to the observed blueshift of the photoresponse. As an illustration, we have plotted a map of the product between the position-dependent absorption spectrum $Abs(r,\lambda)$ and $exp(-r^2/2L_D^2)$, with r the distance to the electrodes. The latter term represents the collection efficiency in a diffusive model. The $Abs(r,\lambda)$ x $exp(-r^2/2L_D^2)$ map is plotted for two values of the diffusion length, and we see an apparent increase of the signal coming from region 1, see **Figure 4**c and d for TM polarization and figure S4 c-d for TE polarization. Finally, we also have plotted the spectral response of the device, taken as the surface integral of the product $Abs(r,\lambda)$ x $exp(-r^2/2L_D^2)$. A blueshift of the resonance is observed for both polarizations (**Figure 4**e and S4e) as the diffusion length is

increased, which corresponds to an increase of the applied bias voltage. More quantitative estimation of the diffusion length from the spectral shift requires considering the vectorial nature of F, $D_0(T)$, and $A(F,T)$, which is beyond the scope of this paper. Eventually, our model also explains the temperature dependence of the shift. At high temperatures, the term $D_0(T)$ prevails in *(1),*[32,33] and only a weak shift is experimentally observed, see **Figure 3***b.* At lower temperatures, the term $D_0(T)$ is reduced, and the field-assisted component $A(F,T).F^2$ then prevails, which explains why a more significant shift is observed at low temperatures.

CONCLUSION

To summarize, we have designed a plasmonic resonator coupled to the short-wave infrared absorption of HgTe NCs. Here, we use a plasmonic resonance to introduce an inhomogeneous electromagnetic field within the NC array. The diffusive transport, often seen as a limitation of NC-based devices, is used to collect the charges over different device areas. Under low field, photogenerated charges are only collected from the region close to the electrodes, where the absorption spectrum is redshifted with respect to that away from the electrodes. In this sense, we fully exploit the interplay between charge transport and optical properties, going beyond the usual approach where cavity resonances are spectrally matched with material absorption[36]. In our case, we engineer the photoconduction by coupling on-demand electromagnetic maps and charge collection through hopping. From this strategy, we obtain a bias tunable photodetector, where the photocurrent peak can be tuned over 15 meV for extended short-wave infrared absorption.

Supporting Information

HgTe NCs synthesis and their characterization, electromagnetic simulation model, tight-binding simulations, device fabrication process, electrical characterization and the description of associated setup, and finally additional data relative to TE polarization.

COMPETING INTEREST

The authors declare no competing financial interests.

ACKNOWLEDGEMENTS

The project is supported by ERC starting grants blackQD (grant n° 756225). We acknowledge the use of clean-room facilities at the “Centrale de Proximité Paris-Centre”. This work has been supported by Region Ile-de-France in the framework of DIM Nano-K (grant dopQD). This work was supported by French state funds managed by the ANR within the Investissements d'Avenir programme under reference ANR-11-IDEX-0004-02 and, more specifically, within the framework of the Cluster of Excellence MATISSE and by grants IPER-Nano2 (ANR-18CE30-0023-01), Copin (ANR-19-CE24-0022), Frontal (ANR-19-CE09-0017), Graskop (ANR-19-CE09-0026), NITQuantum (ANR-20-ASTR-0008-01), Bright and MixDferro. AC thanks Agence Innovation Defense for PhD funding.

REFERENCES

(1) Carey, G. H.; Abdelhady, A. L.; Ning, Z.; Thon, S. M.; Bakr, O. M.; Sargent, E. H. Colloidal Quantum Dot Solar Cells. *Chem. Rev.* **2015**, *115*, 12732–12763.

(2) Nozik, A. . Quantum Dot Solar Cells. *Phys. E Low-dimensional Syst. Nanostructures* **2002**, *14*, 115–120.

(3) Ellingson, R. J.; Beard, M. C.; Johnson, J. C.; Yu, P.; Micic, O. I.; Nozik, A. J.; Shabaev, A.;

Efros, A. L. Highly Efficient Multiple Exciton Generation in Colloidal PbSe and PbS Quantum Dots. *Nano Lett.* **2005**, *5*, 865–871.
(4) Wood, V.; Bulović, V. Colloidal Quantum Dot Light-Emitting Devices. *Nano Rev.* **2010**, *1*, 5202.
(5) Qu, J.; Rastogi, P.; Gréboval, C.; Lagarde, D.; Chu, A.; Dabard, C.; Khalili, A.; Cruguel, H.; Robert, C.; Xu, X. Z.; Ithurria, S.; Silly, M. G.; Ferré, S.; Marie, X.; Lhuillier, E. Electroluminescence from HgTe Nanocrystals and Its Use for Active Imaging. *Nano Lett.* **2020**, *20*, 6185–6190.
(6) Chu, A.; Martinez, B.; Ferré, S.; Noguier, V.; Gréboval, C.; Livache, C.; Qu, J.; Prado, Y.; Casaretto, N.; Goubet, N.; Cruguel, H.; Dudy, L.; Silly, M. G.; Vincent, G.; Lhuillier, E. HgTe Nanocrystals for SWIR Detection and Their Integration up to the Focal Plane Array. *ACS Appl. Mater. Interfaces* **2019**, *11*, 33116–33123.
(7) Rauch, T.; Böberl, M.; Tedde, S. F.; Fürst, J.; Kovalenko, M. V.; Hesser, G.; Lemmer, U.; Heiss, W.; Hayden, O. Near-Infrared Imaging with Quantum-Dot-Sensitized Organic Photodiodes. *Nat. Photonics* **2009**, *3*, 332–336.
(8) Buurma, C.; E. Pimpinella, R.; J. Ciani, A.; S. Feldman, J.; H. Grein, C.; Guyot-Sionnest, P. MWIR Imaging with Low Cost Colloidal Quantum Dot Films. In *Optical Sensing, Imaging, and Photon Counting: Nanostructured Devices and Applications 2016*; 2016; Vol. 9933, p 993303.
(9) Goubet, N.; Jagtap, A.; Livache, C.; Martinez, B.; Portalès, H.; Xu, X. Z.; Lobo, R. P. S. M.; Dubertret, B.; Lhuillier, E. Terahertz HgTe Nanocrystals: Beyond Confinement. *J. Am. Chem. Soc.* **2018**, *140*, 5033–5036.
(10) Tang, X.; Ackerman, M. M.; Shen, G.; Guyot-Sionnest, P. Towards Infrared Electronic Eyes: Flexible Colloidal Quantum Dot Photovoltaic Detectors Enhanced by Resonant Cavity. *Small* **2019**, *15*, 1804920.
(11) Tang, X.; Ackerman, M. M.; Guyot-Sionnest, P. Thermal Imaging with Plasmon Resonance Enhanced HgTe Colloidal Quantum Dot Photovoltaic Devices. *ACS Nano* **2018**, *12*, 7362–7370.
(12) Tang, X.; Ackerman, M. M.; Guyot-Sionnest, P. Acquisition of Hyperspectral Data with Colloidal Quantum Dots. *Laser Photonics Rev.* **2019**, *13*, 1900165.
(13) Chu, A.; Grébova, C.; Goubet, N.; Martinez, B.; Livache, C.; Qu, J.; Rastogi, P.; Bresciani, F. A.; Prado, Y.; Suffit, S.; Ithurria, S.; Vincent, G.; Lhuillier, E. Near Unity Absorption in Nanocrystal Based Short Wave Infrared Photodetectors Using Guided Mode Resonators. *ACS Photonics* **2019**, *6*, 2553–2561.
(14) Rastogi, P.; Chu, A.; Gréboval, C.; Qu, J.; Noumbé, U. N.; Chee, S. S.; Goyal, M.; Khalili, A.; Xu, X. Z.; Cruguel, H.; Ithurria, S.; Gallas, B.; Dayen, J. F.; Dudy, L.; Silly, M. G.; Patriarche, G.; Degiron, A.; Vincent, G.; Lhuillier, E. Pushing Absorption of Perovskite Nanocrystals into the Infrared. *Nano Lett.* **2020**, *20*, 3999–4006.
(15) Gréboval, C.; Chu, A.; Magalhaes, D. V.; Ramade, J.; Qu, J.; Rastogi, P.; Khalili, A.; Chee, S. S.; Aubin, H.; Vincent, G.; Bals, S.; Delerue, C.; Lhuillier, E. Ferroelectric Gating of Narrow Band-Gap Nanocrystal Arrays with Enhanced Light-Matter Coupling. *ACS Photonics* **2021**, *8*, 259–268.
(16) Sergeev, A. A.; Pavlov, D. V.; Kuchmizhak, A. A.; Lapine, M. V.; Yiu, W. K.; Dong, Y.; Ke, N.; Juodkazis, S.; Zhao, N.; Kershaw, S. V.; Rogach, A. L. Tailoring Spontaneous Infrared Emission of HgTe Quantum Dots with Laser-Printed Plasmonic Arrays. *Light Sci. Appl.* **2020**, *9*, 16.
(17) Miller, D. A. B.; Chemla, D. S.; Damen, T. C.; Gossard, A. C.; Wiegmann, W.; Wood, T. H.; Burrus, C. A. Band-Edge Electroabsorption in Quantum Well Structures: The Quantum-Confined Stark Effect. *Phys. Rev. Lett.* **1984**, *53*, 2173–2176.
(18) Empedocles, S. A.; Bawendi, M. G. Quantum-Confined Stark Effect in Single CdSe Nanocrystallite Quantum Dots. *Science.* **1997**, *278*, 2114–2117.
(19) Scott, R.; Achtstein, A. W.; Prudnikau, A. V.; Antanovich, A.; Siebbeles, L. D. A.; Artemyev, M.; Woggon, U. Time-Resolved Stark Spectroscopy in CdSe Nanoplatelets: Exciton Binding Energy, Polarizability, and Field-Dependent Radiative Rates. *Nano Lett.* **2016**, *16*, 6576–6583.
(20) Klem, E. J. D.; Levina, L.; Sargent, E. H. PbS Quantum Dot Electroabsorption Modulation

across the Extended Communications Band 1200-1700 nm. *Appl. Phys. Lett.* **2005**, *87*, 2003–2006.
(21) Walters, G.; Wei, M.; Voznyy, O.; Quintero-Bermudez, R.; Kiani, A.; Smilgies, D. M.; Munir, R.; Amassian, A.; Hoogland, S.; Sargent, E. The Quantum-Confined Stark Effect in Layered Hybrid Perovskites Mediated by Orientational Polarizability of Confined Dipoles. *Nat. Commun.* **2018**, *9*, 4214.
(22) Wang, C.; Shim, M.; Guyot-Sionnest, P. Electrochromic Nanocrystal Quantum Dots. *Science.* **2001**, *291*, 2390–2392.
(23) Shi, X.; Chen, C.; Liu, S.; Li, G. Nonvolatile, Reconfigurable and Narrowband Mid-Infrared Filter Based on Surface Lattice Resonance in Phase-Change $Ge_2Sb_2Te_5$. *Nanomaterials* **2020**, *10*, 2530.
(24) Pogrebnyakov, A. V.; Bossard, J. A.; Turpin, J. P.; Musgraves, J. D.; Shin, H. J.; Rivero-Baleine, C.; Podraza, N.; Richardson, K. A.; Werner, D. H.; Mayer, T. S. Reconfigurable Near-IR Metasurface Based on $Ge_2Sb_2Te_5$ Phase-Change Material . *Opt. Mater. Express* **2018**, *8*, 2264.
(25) Stark, T.; Imboden, M.; Kaya, S.; Mertiri, A.; Chang, J.; Erramilli, S.; Bishop, D. MEMS Tunable Mid-Infrared Plasmonic Spectrometer. *ACS Photonics* **2016**, *3*, 14–19.
(26) Gréboval, C.; Chu, A.; Goubet, N.; Livache, C.; Ithurria, S.; Lhuillier, E. Mercury Chalcogenide Quantum Dots : Material Perspective for Device Integration. *Chem. Rev.* **2021**, *121*, 3627–3700.
(27) Prado, Y.; Qu, J.; Gréboval, C.; Dabard, C.; Rastogi, P.; Chu, A.; Khalili, A.; Xu, X. Z.; Delerue, C.; Ithurria, S.; Lhuillier, E. Seeded Growth of HgTe Nanocrystals for Shape Control and Their Use in Narrow Infrared Electroluminescence. *Chem. Mater.* **2021**, *33*, 2054–2061.
(28) Jouy, P.; Todorov, Y.; Vasanelli, A.; Colombelli, R.; Sagnes, I.; Sirtori, C. Coupling of a Surface Plasmon with Localized Subwavelength Microcavity Modes. *Appl. Phys. Lett.* **2011**, *98*, 021105.
(29) Rastogi, P.; Chu, A.; Dang, T. H.; Prado, Y.; Gréboval, C.; Qu, J.; Dabard, C.; Khalili, A.; Dandeu, E.; Fix, B.; Xu, X. Z.; Ithurria, S.; Vincent, G.; Gallas, B.; Lhuillier, E. Complex Optical Index of HgTe Nanocrystal Infrared Thin Films and Its Use for Short Wave Infrared Photodiode Design. *Adv. Opt. Mater.* **2021**, 9, *2002066*.
(30) Todorov, Y.; Tosetto, L.; Teissier, J.; Andrews, A. M.; Klang, P.; Colombelli, R.; Sagnes, I.; Strasser, G.; Sirtori, C. Optical Properties of Metal-Dielectric-Metal Microcavities in the THz Frequency Range. *Opt. Express* **2010**, *18*, 13886.
(31) Chu, A.; Gréboval, C.; Prado, Y.; Majjad, H.; Delerue, C.; Dayen, J. F.; Vincent, G.; Lhuillier, E. Infrared Photoconduction at the Diffusion Length Limit in HgTe Nanocrystal Arrays. *Nat. Commun.* **2021**, *12*, 1794.
(32) Nenashev, A. V.; Jansson, F.; Baranovskii, S. D.; Österbacka, R.; Dvurechenskii, A. V.; Gebhard, F. Effect of Electric Field on Diffusion in Disordered Materials. II. Two- and Three-Dimensional Hopping Transport. *Phys. Rev. B* **2010**, *81*, 115204.
(33) Nenashev, A. V.; Jansson, F.; Baranovskii, S. D.; Österbacka, R.; Dvurechenskii, A. V.; Gebhard, F. Effect of Electric Field on Diffusion in Disordered Materials. I. One-Dimensional Hopping Transport. *Phys. Rev. B* **2010**, *81*, 115203.
(34) Richert, R.; Pautmeier, L.; Bässler, H. Diffusion and Drift of Charge Carriers in a Random Potential: Deviation from Einsteins Law. *Phys. Rev. Lett.* **1989**, *63*, 547–550.
(35) Arkhipovt, V. I.; Bassler, H. A Model of Weak-Field Quasi-Equilibrium Hopping Transport in Disordered Materials. *Philos. Mag. Lett.* **1993**, *67*, 343–349.
(36) Palaferri, D.; Todorov, Y.; Bigioli, A.; Mottaghizadeh, A.; Gacemi, D.; Calabrese, A.; Vasanelli, A.; Li, L.; Davies, A. G.; Linfield, E. H.; Kapsalidis, F.; Beck, M.; Faist, J.; Sirtori, C. Room-Temperature 9 µm-Wavelength Photo-Detectors and GHz-Frequency Heterodyne Receivers. *Nature* **2018**, *556*, 85–88.

TOC graphic